

Article

Enhanced Photocatalytic Activity of Two-Dimensional Polar Monolayer SiTe for Water-Splitting via Strain Engineering

Di Gu ¹, Wen Qin ¹, Sumei Hu ¹, Rong Li ¹, Xingyuan Chen ^{1,*}, Xiaoma Tao ², Yifang Ouyang ²
and Weiling Zhu ^{1,*}

¹ Department of Physics, School of Science, Guangdong University of Petrochemical Technology, Maoming 525000, China; gudi@gdupt.edu.cn (D.G.)

² School of Physical Science and Technology, Guangxi University, Nanning 530004, China

* Correspondence: chenxingyuan@gdupt.edu.cn (X.C.); zhuweiling@gdupt.edu.cn (W.Z.)

Abstract: A two-dimensional (2D) polar monolayer with a polarization electric field can be used as a potential photocatalyst. In this work, first principle calculations were used to investigate the stability and photocatalytic properties of 2D polar monolayer SiTe as a potential promising catalyst in water-splitting. Our results show that the 2D polar monolayer SiTe possesses an indirect band gap of 2.41 eV, a polarization electric field from the (001) surface to the (00 $\bar{1}$) surface, a wide absorption region, and a suitable band alignment for photocatalytic water-splitting. We also discovered that the photocatalytic activity of 2D polar monolayer SiTe could be effectively tuned through strain engineering. Additionally, strain engineering, particularly compressive strain in the range from -1% to -3% , can enhance the photocatalytic activity of 2D polar monolayer SiTe. Overall, our findings suggest that 2D polar monolayer SiTe has the potential to be a promising catalyst for photocatalytic water-splitting using visible light.

Keywords: polar monolayer SiTe; photocatalytic water-splitting; strain engineering; first principle calculations



Citation: Gu, D.; Qin, W.; Hu, S.; Li, R.; Chen, X.; Tao, X.; Ouyang, Y.; Zhu, W. Enhanced Photocatalytic Activity of Two-Dimensional Polar Monolayer SiTe for Water-Splitting via Strain Engineering. *Molecules* **2023**, *28*, 2971. <https://doi.org/10.3390/molecules28072971>

Academic Editor: Kun Chang

Received: 22 February 2023

Revised: 19 March 2023

Accepted: 23 March 2023

Published: 27 March 2023



Copyright: © 2023 by the authors. Licensee MDPI, Basel, Switzerland. This article is an open access article distributed under the terms and conditions of the Creative Commons Attribution (CC BY) license (<https://creativecommons.org/licenses/by/4.0/>).

1. Introduction

Growing global energy consumption and diminishing fossil fuel reserves have increased concerns about environmental pollution and energy shortages [1]. Renewable and clean energy sources, such as hydrogen [2,3], have become a strategic priority for sustainable development. Since Fujishima's discovery in 1972 that hydrogen can be produced through photocatalysis using titanium dioxide (TiO₂), scientists have assumed that this technology would aid the energy crisis [4]. It is an attractive method for producing hydrogen because it is clean, renewable, and abundant. The technological process of photocatalytic water-splitting requires only water, sunlight, and a catalyst and produces clean and renewable oxygen and hydrogen. The process involves the absorption of light by the photocatalyst, which generates electrons and holes. Therefore, it is considered a prospective technique for solving the pollution problem associated with the energy crisis. However, the efficiency of photocatalytic water-splitting is currently too low for utilization in industries [5,6].

To improve the efficiency of photocatalysis, researchers have focused on addressing the issue of carrier annihilation [7–10]. As we know, carrier annihilation results in the loss of charge carriers, which reduces the efficiency of the reaction. One way to address this problem is to use 2D materials. By reducing the distance that charge carriers need to migrate, the likelihood of carrier annihilation is decreased, and the efficiency of the reaction is improved. These 2D materials, such as g-C₃N₄ [11], group-III monochalcogenide [12], WS₂ Nanosheet [13], MXene [14], and g-ZnO [15], were reported to have had high surface areas and short carrier diffusion lengths, which could effectively reduce the distance that charge carriers need to migrate and improve their efficiency [16–20].

In the recent literature, much research has suggested that 2D polar photocatalysts, which possess a polarization electric field, may be more effective at quickly separating photogenerated carriers [21–24]. There has been growing interest in 2D polar materials, such as group IV materials (GeS [25–27], GeSe [28], SiS [29,30], SiSe [31]), III₂-VI₃ group monolayer In₂Se₃ [32–35], monolayer Al₂OS [36], and monolayer AgBiP₂Se₆, [37] as well as Janus monolayer materials (MoSSe [38–40], PtSSe [41,42], PtSO [43], and WSeTe [44]) for use as photocatalysts, thanks to the electric field that can aid in the separation of excited electron-hole pairs [45–49]. Two-dimensional polar monolayer SiM (M=S, Se and Te) possess high carrier mobility; therefore, they have been reported as potentially promising candidates for photocatalytic water-splitting [30,31,50], especially 2D polar monolayer SiTe, as it has a suitable band gap and absorbs visible light efficiently [50]. However, the effect of the polarization electric field on this material is not yet fully understood. Designing highly efficient catalysts based on 2D polar monolayer materials for photocatalytic water-splitting is critical in developing sustainable energy solutions.

Here, we used the first principles to systematically calculate the stability and photocatalytic properties of 2D polar monolayer SiTe. Our goal was to attain a better comprehension of the potential of this material for use in photocatalytic water-splitting and other applications. Our results show that 2D polar monolayer SiTe exhibits high dynamic, mechanical, and thermal stability. The band gap, band edge positions, and surface potential difference of 2D polar monolayer SiTe are suitable and helpful for water-splitting. Ultraviolet and visible light can be effectively absorbed by 2D polar monolayer SiTe. Furthermore, we found that the properties of 2D polar monolayer SiTe, including its band gap, surface potential difference, polarization electric field, absorption, and photocatalytic activity, can be tuned and enhanced by strain engineering. These findings suggest that 2D polar monolayer SiTe is a promising photocatalyst.

2. Results

Figure 1a shows the top view of the optimized hexagonal honeycomb structure of 2D polar monolayer SiTe, similar to graphene. Figure 1b shows the side view of 2D polar monolayer SiTe, which has a structure with two different layers: the top layer consists of Te atoms, and the bottom layer consists of Si atoms. Two-dimensional polar monolayer SiTe has an unsymmetrical structure along the vertical direction. To determine the most suitable lattice constant for 2D polar monolayer SiTe, we calculated the energy of different lattice constants and plotted the results in Figure S1. The results clearly show that when the lattice constant is 3.83 Å, the 2D polar monolayer SiTe has the lowest energy value, suggesting that it is the most suitable lattice of the monolayer structure. After a full relaxation, the values of the lattice constant, vertical layer distance, and bond distance were calculated, as presented in Table 1. The vertical layer distance is 1.53 Å, and the Si-Te bond distance is 2.69 Å, which are in accordance with previous literature [50–53].

To verify the dynamic stability of the 2D polar monolayer SiTe, we used the density functional perturbation theory method to calculate the phonon dispersion. This allowed us to identify any potential phonon instabilities that could indicate a lack of structural stability in the material. As shown clearly in Figure 1c, all the phonon dispersion modes of 2D polar monolayer SiTe are positive without any imaginary frequency, confirming that the structure of 2D polar monolayer SiTe is dynamically stable. In addition, a 5 × 5 × 1 supercell of 2D polar monolayer SiTe at a temperature of 300 K for a total time of 3000 fs with a time interval of 1 fs was set in the AIMD simulations. As Figure 1d shows, the total energy fluctuation during the dynamic simulations is comparatively small, further indicating the dynamic stability of 2D polar monolayer SiTe.

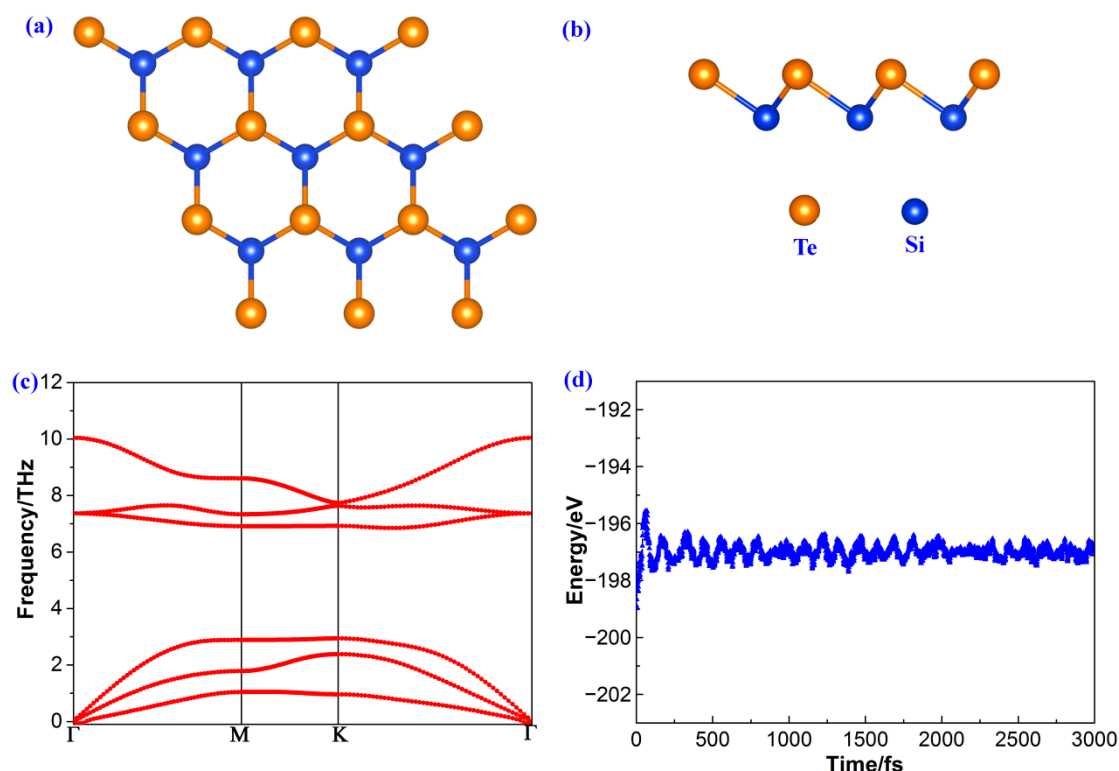


Figure 1. (a) Top view, (b) side view, (c) phonon dispersions, and (d) the total energy fluctuations during AIMD simulations of 2D polar monolayer SiTe.

Table 1. Comparison of the calculated values of lattice constant (a), vertical layer distance (d), bond distance (l), and band gap (E_g).

	a (Å)	d (Å)	l (Å)	E_g (eV)		References
				PBE	HSE06	
	3.83	1.53	2.69	1.80	2.41	This work
SiTe	3.83	1.53	2.69	1.83	2.43	[50]
	3.83	1.53	2.69	1.83	2.36	[51]
	3.83	-	-	1.83	2.49	[52]
	3.835	-	2.690	1.833	-	[53]

The band structure is a significant factor that regulates the photocatalytic activity of a material. The band gap of a photocatalyst should be noteworthy. As shown in Figure 2a, our first principle calculations revealed that the valence band maximum (VBM) of 2D polar monolayer SiTe is at the Γ point. The conduction band minimum (CBM), on the other hand, is situated between the Γ and M points, indicating that 2D polar monolayer SiTe is an indirect semiconductor. Moreover, the band gap of 2D polar monolayer SiTe is 2.41 eV, calculated using the HSE06 functional. This result suggests that ultraviolet light and visible light can be efficiently absorbed by 2D polar monolayer SiTe. As shown in Figure 2b, the VBM of the partial density of states (PDOS) is below the Fermi energy level and is principally provided by the p orbitals of Te and Si atoms, whereas the CBM above the Fermi energy level is primarily provided by the p orbitals of Si atoms. The band gap shown in the PDOS is consistent with that shown in the band structure.

To tune the band structure properties of 2D polar monolayer SiTe effectively, the strain engineering method [54–60] is adopted for the structure of 2D polar monolayer SiTe by controlling the lattice constant of the primitive cell. As shown in Figure S2 and Figure 3, we applied in-plane biaxial strain to 2D polar monolayer SiTe ranging from -5% to $+5\%$ in steps of 1%. Here, a negative sign ($-$) is used to describe the compressive strain. In contrast,

a positive sign (+) is used to describe the tensile strain. As we can see from Figure S2, the band structure of 2D polar monolayer SiTe can be effectively tuned by strain engineering. When a tensile strain from -1% to -5% is applied, the VBM is at the Γ point, and the CBM is situated between the Γ and M points, similar to the band structure without strain engineering. However, when the tensile strain is in the range from $+1\%$ to $+5\%$, the VBM is located between the K and Γ points. As shown in Figure 3, the band gap of 2D polar monolayer SiTe, calculated by the HSE06 method, decreases from 2.41 eV to 1.56 eV as the compressive strain increases from 0 to -5% . For tensile strain, when the strain is $+1\%$, the band gap is 2.44 eV, which is similar to the value without strain engineering. As the strain increases from $+1\%$ to $+5\%$, the band gap decreases from 2.44 eV to 2.23 eV. These results demonstrate that strain engineering would be a feasible technique for controlling and tuning the band structure of 2D polar monolayer SiTe and increasing its activity to absorb solar energy in the ultraviolet and visible light range, which may well strengthen its photocatalytic activity.

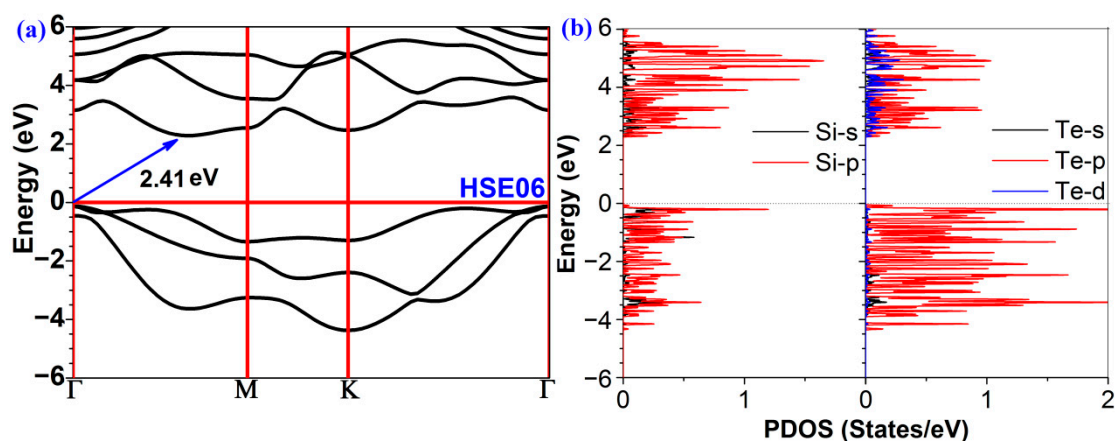


Figure 2. (a) The band structures and (b) the partial density of states (PDOS) of 2D polar monolayer SiTe.

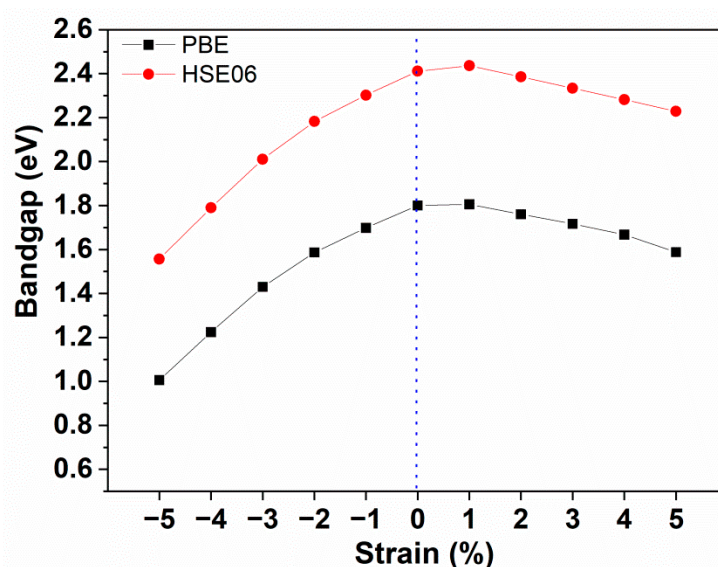


Figure 3. Band gap of 2D polar monolayer SiTe at different strains.

As previously mentioned, 2D polar monolayer SiTe has an unsymmetrical structure along the vertical direction, with a bottom layer of Si atoms and a top layer of Te atoms. As shown in Figure 4a, the difference in electronegativity between Si and Te atoms results in an unsymmetrical planar average potential along the vertical direction. More importantly, the potential of the bottom surface ($00\bar{1}$) is not equal to that of the top surface (001).

According to the theory developed by the Yang group [22], the following equation can be employed to describe the relationship between both the surface potential difference ($\Delta\Phi$) and the polarization electric field (E_{eff}) [22].

$$\Delta\Phi = eE_{eff}d \quad (1)$$

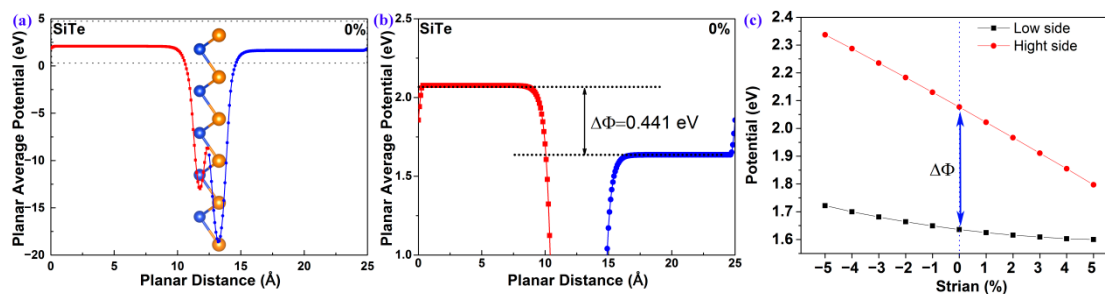


Figure 4. (a) The planar average potential of 2D polar monolayer SiTe; (b) an enlarged section of (a); (c) the surface potential difference ($\Delta\Phi$) of 2D polar monolayer SiTe at different strains.

Here, e is the elementary charge constant, and d is the distance between the Si atomic surface and Te atomic surface.

The larger $\Delta\Phi$, the larger E_{eff} . As shown in Figure 4b, the $\Delta\Phi$, calculated by the surface vacuum energy difference between the Si atomic surface and the Te atomic surface, is 0.441 eV. This indicates that 2D polar monolayer SiTe possesses a polarization electric field E_{eff} , and the direction of the polarization electric field is from the (001) surface to the (00 $\bar{1}$) surface. As we know, the carriers can be separated quickly and irreversibly under the polarization electric field. Therefore the E_{eff} and the $\Delta\Phi$ in 2D polar monolayer SiTe are useful for improving the performance of photocatalytic water-splitting. Additionally, the photocatalyst's band gap E_G , which is required for photocatalytic water-splitting, can be reduced under the effect of the surface potential difference ($\Delta\Phi$) according to the following equation [22],

$$E_G > 1.23 - \Delta\Phi \quad (2)$$

These photocatalysts, such as 2D polar monolayer SiTe, can absorb more solar energy in the infrared and visible region for photocatalytic water-splitting. Therefore, tuning the surface potential difference $\Delta\Phi$ would be an effective and useful way to control photocatalytic activity.

As Figure S3 shows, the planar average potential of 2D polar monolayer SiTe can be regularly controlled by strain engineering. The surface potential difference $\Delta\Phi$ increases under the effect of compressive strain and decreases under the effect of tensile strain. The surface potential difference $\Delta\Phi$ decreases from 0.615 eV to 0.197 eV as the strain engineering increases monotonically from -5% to $+5\%$. Figure 4c shows the changing trends of the surface potential difference $\Delta\Phi$ and the surface vacuum energy (E_{vac}) at different strains. The E_{vac} of both the Si and Te atomic surfaces decreases monotonically with increasing strain engineering from -5% to $+5\%$. Moreover, the E_{vac} decrease trend of the Si atomic surface is obvious, but the E_{vac} decrease trend of the Te atomic surface is slight. The results indicate that the $\Delta\Phi$ of 2D polar monolayer SiTe can be effectively tuned via strain engineering.

To appraise the suitability of 2D polar monolayer SiTe for photocatalytic water-splitting, we calculated its band alignment using the method described in previous studies [21,22]. The band alignment of a material is a critical factor in determining its suitability for photocatalytic water-splitting. For a potential photocatalyst to be effective, the energy level of VBM and CBM must be suitable. As we can see clearly from Figure 5a, the

band alignment of 2D polar monolayer SiTe was calculated by the method reported in the previous literature [22,31]. Firstly, the VBM was calculated by,

$$E_{VBM} = \varphi(\infty) - E_F \quad (3)$$

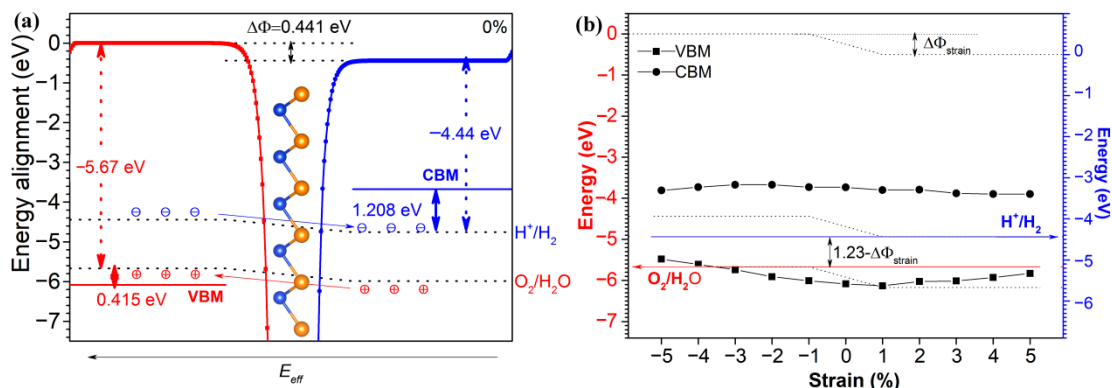


Figure 5. (a) The band alignment of 2D polar monolayer SiTe; (b) the Band alignment as a function of strain engineering.

Here, E_{VBM} is presumed to be the work function throughout this situation. $\varphi(\infty)$ and E_F , respectively, stand in for the Fermi energy level and the vacuum electrostatic potential. Secondly, the CBM was obtained by,

$$E_{CBM} = E_{CBM} + E_g \quad (4)$$

Here, E_g is the band gap shown in Figure 2a.

As shown in Figure 5a, with the vacuum energy level as the reference substance, the reduction potential (H^+/H_2) and the oxidation potential (H_2O/O_2) are -4.44 eV and -5.67 eV, respectively. Since the $\Delta\Phi$ is 0.441 eV in 2D polar monolayer SiTe, the energy level of the (001) surface is not equal to that of the (00 $\bar{1}$) surface. The direction of the polarization electric field E_{eff} is from the (001) surface to the (00 $\bar{1}$) surface. Therefore electrons and holes are moved to the (001) surface and the (00 $\bar{1}$) surface, respectively. On the (001) surface, the H_2O is reduced by the electrons according to the following equation,



In contrast, on the (00 $\bar{1}$) surface, the H_2O is oxidized the holes according to the following equation,



The CBM of 2D polar monolayer SiTe is 1.208 eV higher than the energy level of H^+/H_2 (-4.44 eV), and the VBM is 0.415 eV lower than the energy level of H_2O/O_2 (-5.67 eV). Moreover, under the effect of an electric field E_{eff} , the electrons and holes could be separated quickly; therefore, oxidation and reduction reactions would be carried out efficiently. The results indicated that the band alignment of 2D polar monolayer SiTe is ideal for photocatalytic water-splitting, which involves the production of hydrogen through the use of sunlight and a photocatalyst.

As we can see from Figure S4 and Figure 5b, the CBM of 2D polar monolayer SiTe with strain engineering ranging from -5% to $+5\%$ is higher than the reduction potential level. Compared to the oxidation potential level, the VBM is lower, with strain engineering ranging from -3% to $+5\%$. However, at -5% and -4% compressive strain, the VBM is higher than the magnitude of oxidation potential. This demonstrates that the band alignment of 2D polar monolayer SiTe continues to be well tailored towards photocatalytic water-splitting when strain engineering is applied within the range from -3% to $+5\%$.

The Gibbs free energy difference (ΔG) in the hydrogen reduction was determined using the following equation to investigate the dependence power of total water-splitting [61],

$$\Delta G = \Delta E + \Delta E_{zpe} - T\Delta S \quad (7)$$

Here, ΔE is the adsorption energy, ΔE_{zpe} is the difference in zero-point energy, T is the system temperature (298.15 K, in this work), and ΔS is the entropy difference.

As shown in Figure 6a, the value of ΔG is 1.28 eV. To control and decrease the value of ΔG , strain engineering is adopted to tune the value. As shown in Figure 6b, the ΔG decreases from 1.24 eV to 0.92 eV as the compressive strain decreases from 0 to -3% . For tensile strain, when the strain is $+2\%$, the ΔG is 1.33 eV. As the strain increases from $+2\%$ to $+5\%$, the band gap decreases from 1.33 eV to 1.27 eV regularly. Notably, the value of ΔG can be effectively tuned via strain engineering.

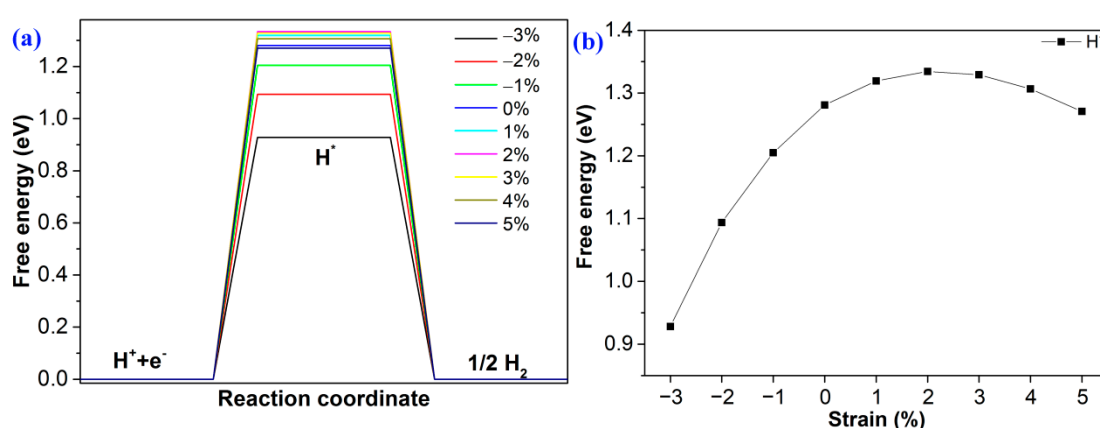


Figure 6. (a) The Gibbs free energy changes of HER at different strains; (b) the trend of ΔG at different strains.

The following equation was used to determine the absorption coefficient $\alpha(\omega)$ of 2D polar monolayer SiTe:

$$\alpha(\omega) = \sqrt{2}\omega \left(\sqrt{(\varepsilon_1(\omega))^2 + (\varepsilon_2(\omega))^2} - \varepsilon_1(\omega) \right)^{\frac{1}{2}} \quad (8)$$

where $\varepsilon_1(\omega)$ and $\varepsilon_2(\omega)$, respectively, represent the real and imaginary components of the dielectric function. As seen from Figure S5a, when the energy is less than 2.00 eV, the absorbance is almost zero. In contrast, when the energy is about 2.50 eV, the absorbance increases dramatically as the energy increases, indicating that some visible light is absorbed efficiently by the 2D polar monolayer SiTe. Moreover, the absorption edge was obtained using the Tauc plot method [62]. As shown in Figure S5b, the band gap E_g , obtained by the optical properties is 2.38 eV, similar to the band gap calculated by the band structures using the HSE06 method. This confirms that the solar light, which has energy larger than the band gap, will be absorbed efficiently by the 2D polar monolayer SiTe. This indicates that 2D polar monolayer SiTe has the potential to be an efficient photocatalyst with high solar energy conversion efficiency. The band gap of 2D polar monolayer SiTe, which is approximately 2.41 eV, plays a role in improving solar energy conversion efficiency. As shown in Figure 7, strain engineering can shift the absorption edge to longer wavelengths, increasing the absorption of visible light. This is due to the decrease in the band gap of 2D polar monolayer SiTe with increasing strain. The results suggest that strain engineering is a convenient and useful strategy for tuning the optical absorption properties of 2D polar monolayer SiTe.

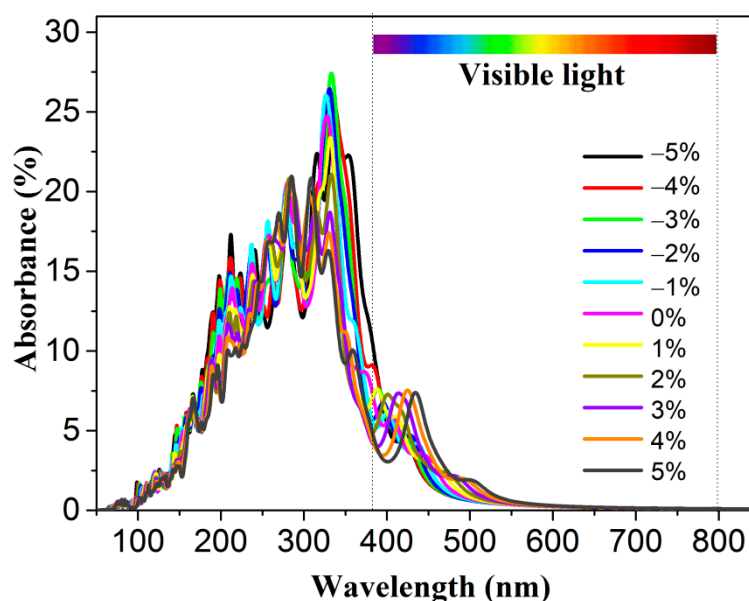


Figure 7. The absorbance of 2D polar monolayer SiTe under strain engineering.

3. Methods

We used the Vienna ab initio simulation package (VASP) [63] with the projector-augmented-wave (PAW) method [64] to calculate the electronic and structural properties of 2D polar monolayer SiTe. To calculate the exchange-correlation energy, the Perdew Burke Ernzerhof (PBE) functional of generalized gradient approximation (GGA) was adopted [65]. The DFT-D3 [66] was utilized to account for long-range van der Waals interactions [67,68]. The PBE method tends to underestimate the band gap, so we also used the HSE06 hybrid functional method [69] to obtain a more accurate band gap value. The plane-wave expansion of the wave function had an energy cutoff of 500 eV. We set the energy convergence and maximum Hellmann–Feynman force convergence criteria to 10^{-6} eV and 10^{-3} eV/Å, respectively. The first integration of the Brillouin zone was performed using the Gamma center method in KPOINTS [70]. Structural optimization and static calculations were performed using $12 \times 12 \times 1$ and $15 \times 15 \times 1$ grids, respectively. The vacuum region in the z direction had a thickness of 20 Å to prevent interactions from the periodic structure. Ab initio molecular dynamics (AIMD) simulations were calculated with the canonical ensemble method [71] to investigate the stability of crystal structure. A $5 \times 5 \times 1$ supercell of 2D polar monolayer SiTe at a temperature of 300 K for a total time of 3000 fs with a time interval of 1 fs was set in the simulations. VASPKIT [72] software was applied to generate electronic data from the raw calculated data.

4. Conclusions

In conclusion, our study, which used first principle calculations, has shown that the 2D polar monolayer SiTe is a potential promising catalyst for water-splitting using visible light. According to the results, the 2D polar monolayer SiTe possesses an indirect band gap of 2.41 eV. The 2D polar monolayer SiTe can absorb ultraviolet and visible light in a wide range. What is more, in the 2D polar monolayer SiTe, the polarization electric field helps to reduce the likelihood of photoinduced electron–hole pair recombination and lower the band gap necessary for water-splitting. The direction of the polarization electric field is from the (001) surface to the (00 $\bar{1}$) surface. The band alignments of 2D polar monolayer SiTe are compatible with the redox potential, making it capable of producing hydrogen and oxygen. Moreover, the electronic, optical, and photocatalytic properties of the 2D polar monolayer SiTe can be controlled and tuned through strain engineering. Additionally, strain engineering, particularly compressive strain in the range from -1% to -3% , can enhance the photocatalytic activity of 2D polar monolayer SiTe. Overall, the suitable band

gap, polarization electric field, and suitable band alignments strongly suggest that the 2D polar monolayer SiTe is a potentially promising, high-efficiency catalyst for photocatalytic water-splitting using visible light.

Supplementary Materials: The following supporting information can be downloaded at: <https://www.mdpi.com/article/10.3390/molecules28072971/s1>, Figure S1: The energy as a function of lattice constant of monolayer SiTe; Figure S2: The band structures of monolayer SiTe under strain engineering; Figure S3: The planar average potential of monolayer SiTe under strain engineering; Figure S4: The band alignment of monolayer SiTe under strain engineering; Figure S5: The Absorbance and Absorption edge of 2D polar monolayer SiTe.

Author Contributions: Conceptualization, D.G. and W.Z.; methodology, D.G., X.C. and X.T.; software, D.G.; validation, D.G., Y.O. and W.Q.; formal analysis, D.G. and R.L.; investigation, D.G. and S.H.; resources, D.G. and W.Z.; data curation, D.G. and W.Z.; writing—original draft preparation, D.G., X.C. and W.Z.; writing—review and editing, D.G., Y.O. and W.Z.; visualization, D.G., X.C. and X.T.; supervision, D.G., Y.O. and R.L.; project administration, D.G., X.C. and W.Z.; funding acquisition, W.Z., S.H. and D.G. All authors have read and agreed to the published version of the manuscript.

Funding: Weiling ZHU thanks the National Natural Science Foundation of China (Grant No. 12074441), Sumei HU thanks the Guangdong Province Special Foundation of Scientific and Technological Innovation (Grant No. 2021S055), and Di GU thanks the Projects of PhDs' Start-up Research of GDUPT (Grant No. 2020bs008) for their financial assistance.

Institutional Review Board Statement: Not applicable.

Informed Consent Statement: Not applicable.

Data Availability Statement: The data that support the findings of this study are available from the corresponding author upon reasonable request.

Conflicts of Interest: The authors declare no conflict of interest.

References

1. Esswein, A.J.; Nocera, D.G. Hydrogen production by molecular photocatalysis. *Chem. Rev.* **2007**, *107*, 4022–4047. [[CrossRef](#)] [[PubMed](#)]
2. Nishiyama, H.; Yamada, T.; Nakabayashi, M.; Maehara, Y.; Yamaguchi, M.; Kuromiya, Y.; Nagatsuma, Y.; Tokudome, H.; Akiyama, S.; Watanabe, T.; et al. Photocatalytic solar hydrogen production from water on a 100-m² scale. *Nature* **2021**, *598*, 304–307. [[CrossRef](#)] [[PubMed](#)]
3. Wang, Z.; Li, C.; Domen, K. Recent developments in heterogeneous photocatalysts for solar-driven overall water splitting. *Chem. Soc. Rev.* **2019**, *48*, 2109–2125. [[CrossRef](#)] [[PubMed](#)]
4. Fujishima, A.; Honda, K. Electrochemical Photolysis of Water at a Semiconductor Electrode. *Nature* **1972**, *238*, 37–38. [[CrossRef](#)] [[PubMed](#)]
5. Li, Y.; Li, Y.; Sa, B.; Ahuja, R. Review of two-dimensional materials for photocatalytic water splitting from a theoretical perspective. *Catal. Sci. Technol.* **2017**, *7*, 545–559. [[CrossRef](#)]
6. Ran, J.; Zhang, J.; Yu, J.; Jaroniec, M.; Qiao, S.Z. Earth-abundant cocatalysts for semiconductor-based photocatalytic water splitting. *Chem. Soc. Rev.* **2014**, *43*, 7787–7812. [[CrossRef](#)]
7. Pan, J.; Shao, X.; Xu, X.; Zhong, J.; Hu, J.; Ma, L. Organic Dye Molecules Sensitization-Enhanced Photocatalytic Water-Splitting Activity of MoS₂ from First-Principles Calculations. *J. Phys. Chem. C* **2020**, *124*, 6580–6587. [[CrossRef](#)]
8. Wang, Y.; Zhang, Y.; Wang, Y.; Zeng, C.; Sun, M.; Yang, D.; Cao, K.; Pan, H.; Wu, Y.; Liu, H.; et al. Constructing van der Waals Heterogeneous Photocatalysts Based on Atomically Thin Carbon Nitride Sheets and Graphdiyne for Highly Efficient Photocatalytic Conversion of CO₂ into CO. *ACS Appl. Mater. Interfaces* **2021**, *13*, 40629–40637. [[CrossRef](#)]
9. Li, S.; Shi, M.; Yu, J.; Li, S.; Lei, S.; Lin, L.; Wang, J. Two-dimensional blue-phase CX (X = S, Se) monolayers with high carrier mobility and tunable photocatalytic water splitting capability. *Chin. Chem. Lett.* **2021**, *32*, 1977–1982. [[CrossRef](#)]
10. Li, J.; Huang, Z.; Ke, W.; Yu, J.; Ren, K.; Dong, Z. High solar-to-hydrogen efficiency in Arsenene/GaX (X = S, Se) van der Waals heterostructure for photocatalytic water splitting. *J. Alloys Compd.* **2021**, *866*, 158774. [[CrossRef](#)]
11. Wang, X.; Maeda, K.; Thomas, A.; Takanabe, K.; Xin, G.; Carlsson, J.M.; Domen, K.; Antonietti, M. A metal-free polymeric photocatalyst for hydrogen production from water under visible light. *Nat. Mater.* **2009**, *8*, 76–80. [[CrossRef](#)]
12. Zhuang, H.L.; Hennig, R.G. Single-Layer Group-III Monochalcogenide Photocatalysts for Water Splitting. *Chem. Mater.* **2013**, *25*, 3232–3238. [[CrossRef](#)]
13. Sang, Y.; Zhao, Z.; Zhao, M.; Hao, P.; Leng, Y.; Liu, H. From UV to near-infrared, WS₂ nanosheet: A novel photocatalyst for full solar light spectrum photodegradation. *Adv. Mater.* **2015**, *27*, 363–369. [[CrossRef](#)] [[PubMed](#)]

14. Guo, Z.; Zhou, J.; Zhu, L.; Sun, Z. MXene: A promising photocatalyst for water splitting. *J. Mater. Chem. A* **2016**, *4*, 11446–11452. [[CrossRef](#)]
15. Huang, B.; Zhou, T.; Wu, D.; Zhang, Z.; Li, B. Properties of vacancies and N-doping in monolayer g-ZnO: First-principles calculation and molecular orbital theory analysis. *Acta Physica Sinica* **2019**, *68*, 246301. [[CrossRef](#)]
16. Bai, Y.; Luo, G.; Meng, L.; Zhang, Q.; Xu, N.; Zhang, H.; Wu, X.; Kong, F.; Wang, B. Single-layer ZnMN₂ (M = Si, Ge, Sn) zinc nitrides as promising photocatalysts. *Phys. Chem. Chem. Phys. PCCP* **2018**, *20*, 14619–14626. [[CrossRef](#)]
17. Jian, C.; Ma, X.; Zhang, J.; Yong, X. Strained MoSi₂N₄ Monolayers with Excellent Solar Energy Absorption and Carrier Transport Properties. *J. Phys. Chem. C* **2021**, *125*, 15185–15193. [[CrossRef](#)]
18. Li, X.; Cui, B.; Zhao, W.; Xu, Y.; Zou, D.; Yang, C. Novel 2D B₂S₃ as a metal-free photocatalyst for water splitting. *Nanotechnol.* **2021**, *32*, 225401. [[CrossRef](#)]
19. Liu, H.; Gao, L.; Xue, Y.; Ye, Y.; Tian, Y.; Jiang, L.; He, S.; Ren, W.; Shai, X.; Wei, T.; et al. Two-dimensional semiconducting Ag₂X (X = S, Se) with Janus-induced built-in electric fields and moderate band edges for overall water splitting. *Appl. Surf. Sci.* **2022**, *597*, 153707. [[CrossRef](#)]
20. Xie, M.; Li, Y.; Liu, X.; Li, X. Enhanced water splitting photocatalyst enabled by two-dimensional GaP/GaAs van der Waals heterostructure. *Appl. Surf. Sci.* **2022**, *591*, 153198. [[CrossRef](#)]
21. Fu, C.; Sun, J.; Luo, Q.; Li, X.; Hu, W.; Yang, J. Intrinsic Electric Fields in Two-dimensional Materials Boost the Solar-to-Hydrogen Efficiency for Photocatalytic Water Splitting. *Nano Lett.* **2018**, *18*, 6312–6317. [[CrossRef](#)] [[PubMed](#)]
22. Li, X.; Li, Z.; Yang, J. Proposed photosynthesis method for producing hydrogen from dissociated water molecules using incident near-infrared light. *Phys. Rev. Lett.* **2014**, *112*, 018301. [[CrossRef](#)] [[PubMed](#)]
23. Li, Z.; Zhang, L.; Liu, Y.; Shao, C.; Gao, Y.; Fan, F.; Wang, J.; Li, J.; Yan, J.; Li, R.; et al. Surface polarity-induced spatial charge separation boosting photocatalytic overall water splitting on GaN nanorod arrays. *Angew. Chem. Int. Ed.* **2019**, *59*, 935–942. [[CrossRef](#)] [[PubMed](#)]
24. Peng, R.; Ma, Y.; Huang, B.; Dai, Y. Two-dimensional Janus PtS₂ for photocatalytic water splitting under the visible or infrared light. *J. Mater. Chem. A* **2019**, *7*, 603–610. [[CrossRef](#)]
25. Ji, Y.; Yang, M.; Dong, H.; Hou, T.; Wang, L.; Li, Y. Two-dimensional germanium monochalcogenide photocatalyst for water splitting under ultraviolet, visible to near-infrared light. *Nanoscale* **2017**, *9*, 8608–8615. [[CrossRef](#)]
26. Gu, D.; Tao, X.; Chen, H.; Ouyang, Y.; Zhu, W.; Du, Y. Two-dimensional polarized MoTe₂/GeS heterojunction with an intrinsic electric field for photocatalytic water-splitting. *RSC Adv.* **2021**, *11*, 34048–34058. [[CrossRef](#)]
27. Gu, D.; Tao, X.; Chen, H.; Zhu, W.; Ouyang, Y.; Du, Y.; Peng, Q. Highly Efficient Polarized GeS/MoSe₂ van der Waals Heterostructure for Water Splitting from Ultraviolet to Near-Infrared Light. *Physica Status Solidi (RRL)–Rapid Res. Lett.* **2020**, *14*, 1900582. [[CrossRef](#)]
28. Gu, D.; Tao, X.; Chen, H.; Zhu, W.; Ouyang, Y.; Peng, Q. Enhanced photocatalytic activity for water splitting of blue phase GeS and GeSe monolayers via biaxial straining. *Nanoscale* **2019**, *11*, 2335–2342. [[CrossRef](#)] [[PubMed](#)]
29. Abid, A.; Idrees, M.; Din, H.U.; Alam, Q.; Amin, B.; Haneef, M. Structural, electronic, optical, thermoelectric and photocatalytic properties of SiS/MXenes van der Waals heterostructures. *Mater. Today Commun.* **2021**, *26*, 101702. [[CrossRef](#)]
30. Alam, Q.; Muhammad, S.; Idrees, M.; Hieu, N.V.; Binh NT, T.; Nguyen, C.; Amin, B. First-principles study of the electronic structures and optical and photocatalytic performances of van der Waals heterostructures of SiS, P and SiC monolayers. *RSC Adv.* **2021**, *11*, 14263–14268. [[CrossRef](#)]
31. Gu, D.; Chen, X.; Xu, X.; Qin, W.; Tao, X.; Ouyang, Y.; Zhu, W. Polarization Electric Field in 2D Polar Monolayer Silicon Monochalcogenides SiX (X = S, Se) as Potential Photocatalysts for Water Splitting. *Physica Status Solidi (RRL)–Rapid Res. Lett.* **2022**, *17*, 2200179. [[CrossRef](#)]
32. Ding, W.; Zhu, J.; Wang, Z.; Gao, Y.; Xiao, D.; Gu, Y.; Zhang, Z.; Zhu, W. Prediction of intrinsic two-dimensional ferroelectrics in In₂Se₃ and other III₂-VI₃ van der Waals materials. *Nat. Commun.* **2017**, *8*, 14956. [[CrossRef](#)] [[PubMed](#)]
33. Xiao, J.; Zhu, H.; Wang, Y.; Feng, W.; Hu, Y.; Dasgupta, A.; Han, Y.; Wang, Y.; Muller, D.A.; Martin, L.W.; et al. Intrinsic Two-Dimensional Ferroelectricity with Dipole Locking. *Phys. Rev. Lett.* **2018**, *120*, 227601. [[CrossRef](#)]
34. Zhao, P.; Ma, Y.; Lv, X.; Li, M.; Huang, B.; Dai, Y. Two-dimensional III₂-VI₃ materials: Promising photocatalysts for overall water splitting under infrared light spectrum. *Nano Energy* **2018**, *51*, 533–538. [[CrossRef](#)]
35. Zhou, Y.; Wu, D.; Zhu, Y.; Cho, Y.; He, Q.; Yang, X.; Herrera, K.; Chu, Z.; Han, Y.; Downer, M.C.; et al. Out-of-Plane Piezoelectricity and Ferroelectricity in Layered alpha-In₂Se₃ Nanoflakes. *Nano Lett.* **2017**, *17*, 5508–5513. [[CrossRef](#)]
36. Haman, Z.; Khossossi, N.; Kibbou, M.; Bouziani, I.; Singh, D.; Essaoudi, I.; Ainane, A.; Ahuja, R. Janus Aluminum Oxysulfide Al₂OS: A promising 2D direct semiconductor photocatalyst with strong visible light harvesting. *Appl. Surf. Sci.* **2022**, *589*, 152997. [[CrossRef](#)]
37. Ju, L.; Shang, J.; Tang, X.; Kou, L. Tunable Photocatalytic Water Splitting by the Ferroelectric Switch in a 2D AgBiP₂Se₆ Monolayer. *J. Am. Chem. Soc.* **2020**, *142*, 1492–1500. [[CrossRef](#)]
38. Ma, X.; Wu, X.; Wang, H.; Wang, Y. A Janus MoSSe monolayer: A potential wide solar-spectrum water-splitting photocatalyst with a low carrier recombination rate. *J. Mater. Chem. A* **2018**, *6*, 2295–2301. [[CrossRef](#)]
39. Zhao, F.; Li, J.; Chen, Y.; Zhang, M.; Zhang, H. Photocatalytic activity of co-doped Janus monolayer MoSSe for solar water splitting: A computational investigation. *Appl. Surf. Sci.* **2021**, *544*, 148741. [[CrossRef](#)]

40. Ji, Y.; Yang, M.; Lin, H.; Hou, T.; Wang, L.; Li, Y.; Lee, S.T. Janus Structures of Transition Metal Dichalcogenides as the Heterojunction Photocatalysts for Water Splitting. *J. Phys. Chem. C* **2018**, *122*, 3123–3129. [[CrossRef](#)]
41. Wang, G.; Tang, W.; Xie, W.; Tang, Q.; Wang, Y.; Guo, H.; Gao, P.; Dang, S.; Chang, J. Type-II CdS/PtS₂ heterostructures used as highly efficient water-splitting photocatalysts. *Appl. Surf. Sci.* **2022**, *589*, 152931. [[CrossRef](#)]
42. Wang, G.; Tang, W.; Xu, C.; He, J.; Zeng, Q.; Xie, W.; Gao, P.; Chang, J. Two-dimensional CdO/PtS₂ heterojunctions used for Z-scheme photocatalytic water-splitting. *Appl. Surf. Sci.* **2022**, *599*, 153960. [[CrossRef](#)]
43. Shen, H.N.; Zhang, Y.; Wang, G.Z.; Ji, W.X.; Xue, X.M.; Zhang, W. Janus PtXO (X = S, Se) monolayers: The visible light driven water splitting photocatalysts with high carrier mobilities. *Phys. Chem. Chem. Phys. PCCP* **2021**, *23*, 21825–21832. [[CrossRef](#)]
44. Jamdagni, P.; Pandey, R.; Tankeshwar, K. First principles study of Janus WSeTe monolayer and its application in photocatalytic water splitting. *Nanotechnol.* **2022**, *33*, 025703. [[CrossRef](#)] [[PubMed](#)]
45. Chen, F.; Huang, H.; Guo, L.; Zhang, Y.; Ma, T. The Role of Polarization in Photocatalysis. *Angew. Chem. Int. Ed.* **2019**, *58*, 10061–10073. [[CrossRef](#)] [[PubMed](#)]
46. Liang, Y.; Li, J.; Jin, H.; Huang, B.; Dai, Y. Photoexcitation Dynamics in Janus-MoSSe/WSe₂ Heterobilayers: Ab Initio Time-Domain Study. *J. Phys. Chem. Lett.* **2018**, *9*, 2797–2802. [[CrossRef](#)] [[PubMed](#)]
47. Liu, L.; Huang, H. Ferroelectrics in Photocatalysis. *Chemistry* **2022**, *28*, e202103975. [[CrossRef](#)] [[PubMed](#)]
48. Yin, W.; Wen, B.; Ge, Q.; Zou, D.; Xu, Y.; Liu, M.; Wei, X.; Chen, M.; Fan, X. Role of intrinsic dipole on photocatalytic water splitting for Janus MoSSe/nitrides heterostructure: A first-principles study. *Prog. Nat. Sci.: Mater. Int.* **2019**, *29*, 335–340. [[CrossRef](#)]
49. Jiang, X.X.; Gao, Q.; Xu, X.H.; Xu, G.; Li, D.M.; Cui, B.; Liu, D.S.; Qu, F.Y. Design of a noble-metal-free direct Z-scheme photocatalyst for overall water splitting based on a SnC/SnSSe van der Waals heterostructure. *Phys. Chem. Chem. Phys. PCCP* **2021**, *23*, 21641–21651. [[CrossRef](#)]
50. Zhu, Y.L.; Yuan, J.H.; Song, Y.Q.; Wang, S.; Xue, K.H.; Xu, M.; Cheng, X.M.; Miao, X.S. Two-dimensional silicon chalcogenides with high carrier mobility for photocatalytic water splitting. *J. Mater. Sci.* **2019**, *54*, 11485–11496. [[CrossRef](#)]
51. Chen, Y.; Sun, Q.; Jena, P. SiTe monolayers: Si-based analogues of phosphorene. *Journal of Materials Chemistry C* **2016**, *4*, 6353–6361. [[CrossRef](#)]
52. Bhattarai, R.; Shen, X. Optical and electronic properties of SiTe_x (x = 1, 2) from first-principles. *J. Appl. Phys.* **2021**, *129*, 224305. [[CrossRef](#)]
53. Kamal, C.; Chakrabarti, A.; Ezawa, M. Direct band gaps in group IV-VI monolayer materials: Binary counterparts of phosphorene. *Phys. Rev. B* **2016**, *93*, 125428. [[CrossRef](#)]
54. Chen, X.; Han, W.; Jia, M.; Ren, F.; Peng, C.; Gu, Q.; Wang, B.; Yin, H. A direct Z-scheme MoSi₂N₄/BlueP vdW heterostructure for photocatalytic overall water splitting. *J. Phys. D: Appl. Phys.* **2022**, *55*, 215502. [[CrossRef](#)]
55. Gu, D.; Tao, X.; Chen, H.; Ouyang, Y.; Zhu, W.; Peng, Q.; Du, Y. Strain Enhanced Visible-Ultraviolet Absorption of Blue Phosphorene/MoX₂ (X = S, Se) Heterolayers. *Physica Status Solidi (RRL)–Rapid Res. Lett.* **2019**, *13*, 1800659. [[CrossRef](#)]
56. Zhao, H.Y.; Li, E.L.; Liu, C.; Shen, Y.; Shen, P.F.; Cui, Z.; Ma, D.M. DFT computation of two-dimensional CdO/GaS van der Waals heterostructure: Tunable absorption spectra for water splitting application. *Vacuum* **2021**, *192*, 110434. [[CrossRef](#)]
57. Ren, K.; Shu, H.B.; Huo, W.Y.; Cui, Z.; Yu, J.; Xu, Y.J. Mechanical, electronic and optical properties of a novel B₂P₆ monolayer: Ultrahigh carrier mobility and strong optical absorption. *Phys. Chem. Chem. Phys. PCCP* **2021**, *23*, 24915–24921. [[CrossRef](#)] [[PubMed](#)]
58. Ren, K.; Yu, J.; Tang, W. Two-dimensional ZnO/BSe van der waals heterostructure used as a promising photocatalyst for water splitting: A DFT study. *J. Alloys Compd.* **2020**, *812*, 152049. [[CrossRef](#)]
59. Yang, X.; Zhou, Y.; He, J. Two unexplored two-dimensional MSe₂ (M = Cd, Zn) structures as the photocatalysts of water splitting and the enhancement of their performances by strain. *Vacuum* **2020**, *182*, 109728. [[CrossRef](#)]
60. Xu, F.Y.; Zhou, Y.; Zhang, T.; Zeng, Z.Y.; Chen, X.R.; Geng, H.Y. An ab initio study of two-dimensional anisotropic monolayers ScXY (X = S and Se; Y = Cl and Br) for photocatalytic water splitting applications with high carrier mobilities. *Phys. Chem. Chem. Phys. PCCP* **2022**, *24*, 3770–3779. [[CrossRef](#)]
61. Nørskov, J.K.; Rossmeisl, J.; Logadottir, A.; Lindqvist, L.; Kitchin, J.R.; Bligaard, T.; Jónsson, H. Origin of the Overpotential for Oxygen Reduction at a Fuel-Cell Cathode. *J. Phys. Chem. B* **2004**, *108*, 17886–17892. [[CrossRef](#)]
62. Tauc, J.; Grigorovici, R.; Vancu, A. Optical Properties and Electronic Structure of Amorphous Germanium. *Phys. Status Solidi (B)* **1966**, *15*, 627–637. [[CrossRef](#)]
63. Kresse, G.; Furthmüller, J. Efficient iterative schemes for ab initio total-energy calculations using a plane-wave basis set. *Phys. Rev. B* **1996**, *54*, 11169–11186. [[CrossRef](#)]
64. Blochl, P.E. Projector augmented-wave method. *Phys. Rev. B* **1994**, *50*, 17953–17979. [[CrossRef](#)]
65. Perdew, J.P.; Burke, K.; Ernzerhof, M. Generalized gradient approximation made simple. *Phys. Rev. Lett.* **1996**, *77*, 3865–3868. [[CrossRef](#)]
66. Grimme, S. Semiempirical GGA-type density functional constructed with a long-range dispersion correction. *J. Comput. Chem.* **2006**, *27*, 1787–1799. [[CrossRef](#)] [[PubMed](#)]
67. Klimeš, J.; Bowler, D.R.; Michaelides, A. Chemical accuracy for the van der Waals density functional. *J. Phys. Condens. Matter* **2009**, *22*, 022201. [[CrossRef](#)] [[PubMed](#)]
68. Klimeš, J.; Bowler, D.R.; Michaelides, A. Van der Waals density functionals applied to solids. *Phys. Rev. B* **2011**, *83*, 195131. [[CrossRef](#)]

69. Paier, J.; Marsman, M.; Hummer, K.; Kresse, G.; Gerber, I.C.; Angyan, J.G. Screened hybrid density functionals applied to solids. *J. Chem. Phys.* **2006**, *124*, 154709. [[CrossRef](#)]
70. Monkhorst, H.J.; Pack, J.D. Special points for Brillouin-zone integrations. *Phys. Rev. B* **1976**, *13*, 5188–5192. [[CrossRef](#)]
71. Martyna, G.J.; Klein, M.L.; Tuckerman, M. Nosé-Hoover chains: The canonical ensemble via continuous dynamics. *J. Chem. Phys.* **1992**, *97*, 2635–2643. [[CrossRef](#)]
72. Wang, V.; Xu, N.; Liu, J.C.; Tang, G.; Geng, W.T. VASPKIT: A user-friendly interface facilitating high-throughput computing and analysis using VASP code. *Comput. Phys. Commun.* **2021**, *267*, 108033. [[CrossRef](#)]

Disclaimer/Publisher’s Note: The statements, opinions and data contained in all publications are solely those of the individual author(s) and contributor(s) and not of MDPI and/or the editor(s). MDPI and/or the editor(s) disclaim responsibility for any injury to people or property resulting from any ideas, methods, instructions or products referred to in the content.